



# A titanium-nitrogen alloy with ultrahigh strength by ball milling and spark plasma sintering

Jiayin Chen<sup>a,1</sup>, Zeyun Cai<sup>a,1</sup>, Tao Xiang<sup>a</sup>, Peng Du<sup>a</sup>, Guoqiang Xie<sup>a,b,\*</sup>

<sup>a</sup> School of Materials Science and Engineering, Harbin Institute of Technology (Shenzhen), Shenzhen, 518055, China

<sup>b</sup> State Key Laboratory of Advanced Welding and Joining, Harbin Institute of Technology, Harbin, 150001, China



## ARTICLE INFO

### Keywords:

Ti-N alloy  
Solid solution strengthening  
Ultra-high yield strength  
Ball milling  
Spark plasma sintering

## ABSTRACT

The high strength and low cost of titanium alloys have led to the development of these alloys for aerospace applications. In this study, ultra-high-strength Ti-N alloys were fabricated by ball-milling (BM) and spark plasma sintering (SPS), and the effects of the nitrogen content on the microstructure and mechanical properties of the alloys were studied. TiN powder was used as the raw material for doping the alloys with N atoms, and the N content was controlled by tuning the amount of TiN powder added. The yield strength of the Ti-N alloys increased with an increase in the N content and surpassed 2000 MPa when the N content reached 2.66 wt%. Quantitative analysis using the Hall-Petch equation and Labusch model demonstrated that fine-grain strengthening and solution strengthening worked in synergy to enhance the strength of the Ti-N alloys. The ultra-high-strength Ti-N alloys can be applied in the aerospace field for structure use, such as aircraft engines, fasteners, and burn-resistant materials. The preparation of novel Ti-N alloys validates the theoretical application of ubiquitous elements in titanium alloys.

## 1. Introduction

Titanium and its alloys are well known for their excellent mechanical properties, outstanding biocompatibility, superior corrosion resistance, and high specific strength-to-weight ratio [1–3]. Thus, these alloys are widely applied in many fields, particularly in aerospace environments. For example, the exceptional thermal expansion coefficient and galvanic corrosion resistance of titanium materials match the engineering requirements of spacecraft [4,5]. Furthermore, the high specific strength-to-weight ratio enables a significant reduction in the weight of titanium and its alloys, rendering these materials effective substitutes for steel [7] in aircraft engines, fuselage, and landing gear [6]. As a structural component, titanium comprises up to 9 wt% of the Boeing 777 aircraft, and its ratio is predicted to increase in the future [7]. For example, more than 40 wt% titanium is used in advanced battle planes such as the F22 [8]. The global aerospace materials market is expected to reach 25.80 billion USD by 2022 [9]. Therefore, sustainable development of the aerospace industry is expected to lead to increased consumption of titanium and its alloys.

Materials with higher strength, lower density, and better machinability for aerospace applications have been constantly pursued for a

considerable period [10,11]. Improving the strength of these materials can further enhance the specific strength-to-weight ratio, which offers the opportunity for weight reduction in applications. For example, in the landing gear on the Boeing 777, all the labeled parts were fabricated from Ti-10V-2Fe-3Al, as a replacement for the low-alloy steel, enabling the weight of the gear to be reduced by 580 kg [12]. Thus, the development of high-strength titanium alloys and further research have been a significant focus for a long time.

Incorporating alloying elements is a common method for enhancing the strength of titanium. Ti and its alloys can be classified as  $\alpha$ , near- $\alpha$ ,  $\alpha + \beta$ , metastable  $\beta$ , or stable  $\beta$  according to their microstructure at room temperature. Elements such as nitrogen, oxygen, and carbon, which stabilize the  $\alpha$  phase, are  $\alpha$ -stabilizing elements, compared to the  $\beta$ -stabilizing elements that stabilize the  $\beta$  phase, such as niobium, vanadium, and chromium [13]. The yield strength of traditional titanium alloys is approximately 600–1000 MPa, and  $\beta$ -Ti has become a popular research target owing to its relatively good yield strength and low Young's modulus [14–16]. On the other hand, the low thermal conductivity and low modulus of elasticity cause problems in machining titanium alloys, leading to difficulty in industrial production [17]. Moreover, the cost of  $\beta$ -Ti structural materials cannot be ignored. Many  $\beta$ -stabilizing elements

\* Corresponding author. School of Materials Science and Engineering, Harbin Institute of Technology (Shenzhen), Shenzhen, 518055, China.

E-mail address: [xieguoqiang@hit.edu.cn](mailto:xieguoqiang@hit.edu.cn) (G. Xie).

<sup>1</sup> J.Y. Chen and Z.Y. Cai can be considered as co-first authors.

provide excellent properties but are accompanied by a high price.

Considering the problems mentioned above, some researchers have investigated the strengthening effect of ubiquitous elements such as nitrogen and oxygen on titanium alloys [18–26]. These are  $\alpha$ -stabilizing elements, resulting in titanium alloys that are hardened with better thermal stability and a higher modulus of elasticity than  $\beta$ -Ti. In addition, ubiquitous elements are generally low cost and nontoxic. Generally, the yield strength of Ti alloys increases with increasing N content. N atoms exhibit a better strengthening effect compared with O atoms. But there are few studies on the effect of N atoms in titanium alloys; one of the reasons for this is that the solubility of N atoms in titanium is low, and the metal nitride forms when the N content exceeds 19 at%. Pure titanium exhibits superior ductility compared with Ti-6Al-4V, a common titanium alloy on the market [27]. Therefore, pure titanium is generally chosen as the research object. Powder metallurgy (PM) effectively introduces ubiquitous elements into titanium alloys and can reduce the cost of alloy components as a near-net-shaped method. Using spark plasma sintering (SPS), Mimoto et al. [28] sintered N-solute powders prepared by a gas ( $N_2$ )–solid (Ti starting powder) direct reaction process. As a compression technique for fabricating bulk materials, SPS has the advantage of rapid heating and cooling, which can prevent grain coarsening due to the short sintering time [29,30]. However, the researchers found that the non-uniform distribution of N atoms led to the formation of a nitride layer ( $Ti_2N$ ) on the material surface, which required a solid-state consolidation process to dissolve the N atoms and hot extrusion to densify the alloys. Moreover, the highest N content was only approximately 0.9 wt% in CP-Ti after 180 min of  $N_2$  gas treatment, and there was no specific compressive test fracture analysis.

Based on the PM technology, this study provides a one-step process for fabricating high-strength and low-cost titanium alloys. First, mixed powders of CP-Ti and x wt% TiN (x = 0, 2, 4, 6, 8) are consolidated by ball-milling via SPS, after which five titanium alloys with different N contents are prepared successfully. The TiN powder as the N source can avoid the nitride layer formation after  $N_2$  gas treatment. The formation of the nitride layer prevents the further diffusing of N atoms, and the N content is limited in this way. By changing the addition of TiN powder, the N content can be regulated simply. The fracture mode was systematically analyzed by observing the fracture surface of the samples after compressive tests. The strengthening mechanism was also given through the quantitative calculation of the yield strength. The Ti-N alloys' fabrication and research aim to promote the development of ubiquitous application elements in titanium alloy for aerospace use.

## 2. Materials and experimental procedures

### 2.1. Raw materials

Commercially pure Ti powder (99.99%, Shanghai Aladdin Biochemical Technology Co.) and TiN powder (99.5%, Beijing Inno-Chem Science & Technology Co., Ltd.) were used as raw materials in this study. A laser scattering particle size distribution analyzer (MS 3000, Malvern Panalytical Ltd.) was used to measure the average diameters of the Ti and TiN powders. The particle morphology was observed using a field-emission scanning electron microscope (FESEM, ZEISS SUPRA55, Carl Zeiss).

Ti powder and x wt% (x = 0, 2, 4, 6, 8) TiN powder were mixed using a planetary ball-mill (QM-3SP2, Nanjing Chi Shun Technology Development Co., Ltd.) at 250 rpm for 2 h; the ball-milling parameters were selected according to a previous study [26]. The ball-milling jar was made of zirconia, and its volume was approximately 250 mL. Four types of zirconia balls were used: one with a mass of 57.0 g, two with masses of 25.7 g, sixteen with masses of 5.6 g, and fifteen with masses of 1.8 g. The ball-to-powder ratio was 5:1. The jar was filled with argon gas to remove air.

### 2.2. Processing

After ball-milling, a graphite mold with a diameter of 36 mm was filled with 23 g of the milled powder, which was consolidated using SPS (SPS-20T-10-IV, Shanghai Chenhua Science Technology Corp., Ltd.) at 1273 K for 30 min at a pressure of 30 MPa under vacuum. The details of the SPS process are described in our previous work [26]. After cooling in the furnace, the sintered samples with a diameter of 36 mm and a length of 4.5 mm were obtained (denoted as Ti + 0TiN, Ti + 2TiN, Ti + 4TiN, Ti + 6TiN, and Ti + 8TiN). Specific process details, including ball milling, filling, and spark plasma sintering, are shown in Fig. 1(a). A schematic of the detailed processes for fabricating the desired samples is presented in Fig. 1(b).

### 2.3. Characterization

A hydrogen analyzer (LECO RHEN602, Laboratory Equipment Corporation), carbon analyzer (LECO CS3000, Laboratory Equipment Corporation), and an O/N analyzer (LECO ON836, Laboratory Equipment Corporation) were used to measure the content of the light elements, i.e., nitrogen, oxygen, hydrogen, carbon. Specifically, the N, O, and H content was measured using two sample rods with a diameter of 3 mm and length of 50 mm, while a 4 g specimen was used for C content analysis. X-ray diffraction (XRD, Aries, Malvern Panalytical Ltd.) was used to determine the phase constitutions of the mixed powders and sintered samples using Cu-K $\alpha$  radiation ( $\lambda = 0.154$  nm) at 40 kV in the 2 $\theta$  range of 20–80°. The lattice parameters along the a-axis and c-axis were calculated from the XRD data by Software Jade 6.5, based on the equation of the interplanar crystal spacing for a hexagonal close packed (HCP) structure ( $\frac{1}{d_{hkl}^2} = \frac{4(h^2 + hk + k^2)}{3a^2} + \frac{l^2}{c^2}$ ) and Bragg's law ( $2d_{hkl} \sin\theta = \lambda$ ) [31]. A field-emission scanning electron microscope (FESEM, ZEISS SUPRA55, Carl Zeiss) was used to observe the milled powders and fracture surfaces' morphology (ETH = 5.0 kV). Electron backscattered diffraction (EBSD, Oxford symmetry, Oxford Instruments) was used to examine the grain sizes and distributions of the specimens, which were polished using an ion thinning meter (Gatan 695, Gatan, Inc.). A universal testing machine (AGX-50kNVD, Shimadzu Corporation) was used to evaluate the mechanical properties at ambient temperature under a strain rate of  $5.0 \times 10^{-4}$  s $^{-1}$ . In preparing the sample for the compressive test, specimens with dimensions of 2 mm × 2 mm × 4 mm were machined from the sintered samples and ground using 2000-mesh SiC sandpaper. At least four compressive specimens were machined for each sample to obtain the average value. An ultrasonic system was used to accurately measure the elastic constants of the sintered samples.

## 3. Results

### 3.1. Characterization of powders

Fig. 2(a and b) shows SEM images and distribution of the particle size of the raw Ti and TiN powders. The raw Ti powders with a surface area average particle size D (3, 2) of  $25.7 \pm 0.1$   $\mu$ m appeared irregular, whereas the raw TiN powders appeared irregular with a smaller average particle size of  $1.7 \pm 0.1$   $\mu$ m. The ball-milling process affects the uniformity of the powders. After ball-milling, the TiN particles were dispersed around the Ti particles, and the surface area average particle size of the mixed powder was  $23.8 \pm 0.8$   $\mu$ m, as shown in Fig. 2(c). The XRD patterns of the mixed powders (Fig. 3) indicate that no other microstructural phases were present, except for  $\alpha$ -Ti and TiN. By comparing the XRD patterns of each batch of mixed powder, no bands were found to shift at any angle, and the intensity of the TiN peaks increased with the addition of TiN, indicating that there was no expansion in the crystal lattice and no chemical reaction of TiN.

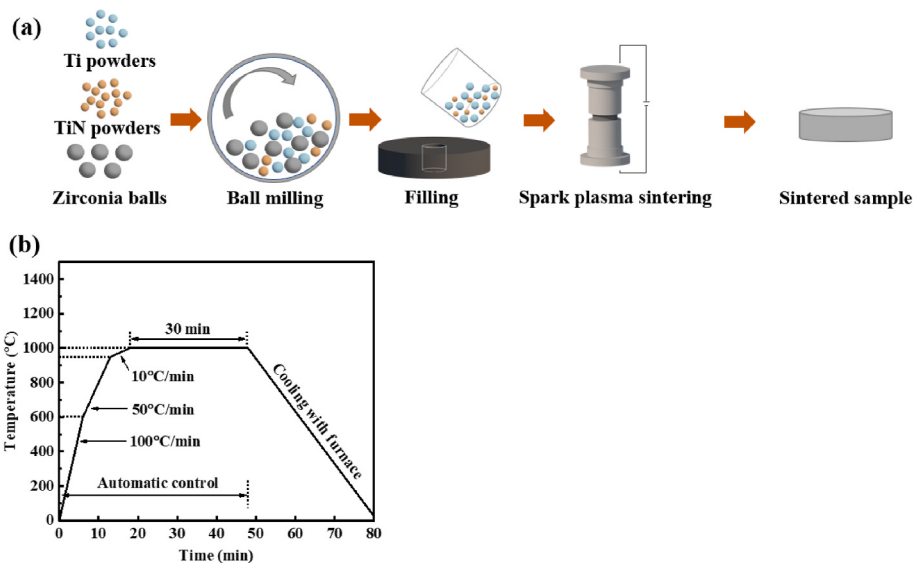


Fig. 1. Schematic diagrams of (a) fabricating processes, (b) sintering parameters.

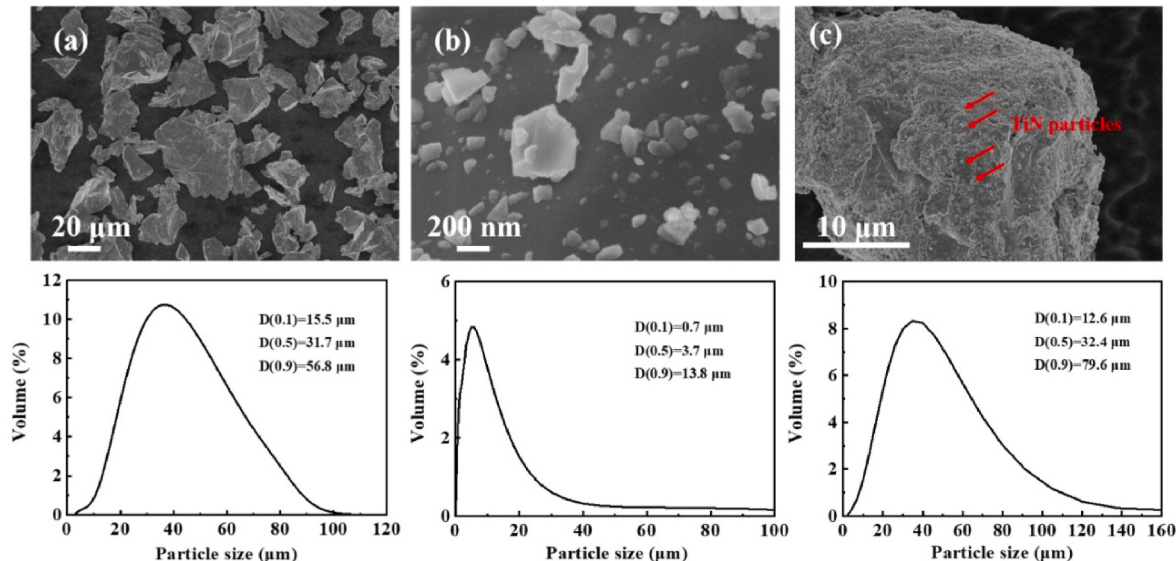


Fig. 2. SEM images and particle size distribution graphs of (a) the raw pure Ti powder, (b) the raw TiN powder, (c) the mixed Ti and TiN powders.

### 3.2. Phase and microstructure of the sintered Ti-N alloys

The mixed powders of Ti and TiN were consolidated using SPS, and sintered samples were obtained. Table 1 lists the N, O, H, and C content of the sintered samples. Note that ubiquitous elements would inevitably be introduced during the ball-milling and sintering processes; thus, the accurate content of these elements might not be the same as the theoretical content. The O, C, and H contents were almost identical for all the Ti-N alloys, with values of 0.4, 0.01, and 0.1 wt%, respectively. However, the N content ranged from 0.63 to 2.66 wt%, which is below the maximum solubility of N atoms in titanium and ten times higher than that of the other ubiquitous elements. In this study, the N content was as high as 2.66 wt%, which is two times higher than that in the previous studies (0.89 wt%) [32]. Therefore, it was concluded that N atoms were introduced into the Ti matrix by adding TiN powder.

The XRD patterns of the sintered samples are shown in Fig. 4. Only peaks of Ti with an HCP structure were found, and no other compounds were detected, including TiN. Due to the concentration difference, there is a trend that the N atoms diffuse from TiN to Ti. In SPS, the plasma

generates around the contact points of powder particles. Thus, the actual temperature at the sintering neck is higher than the bulk temperature, which provides more energy to drive the diffusion [33]. In addition, because of the internal stress relaxation during the sintering, the interface between the solid-solid phase melts at the nanoscale at temperature hundreds of degrees below the melting temperature, reducing the resistance of diffusion [34,35]. Therefore, it is suggested that the N atoms dissolved in the  $\alpha$ -Ti matrix as solute atoms. A previous study also reported a similar phenomenon when titanium alloys were treated under nitrogen at high temperatures [36]. Furthermore, the (0002)  $\alpha$ -Ti peak shifted significantly toward a lower diffraction angle with increasing addition of TiN, while the diffraction angle of the (10 1(-) 0)  $\alpha$ -Ti peak remained the same.

### 3.3. Physical and mechanical properties of the sintered samples

The inverse pole figure (IPF) maps for the Ti-N alloys analyzed by EBSD are shown in Fig. 5. All the sintered Ti-N samples consisted of equiaxed  $\alpha$ -Ti grains without acicular grains. The red, blue, and green

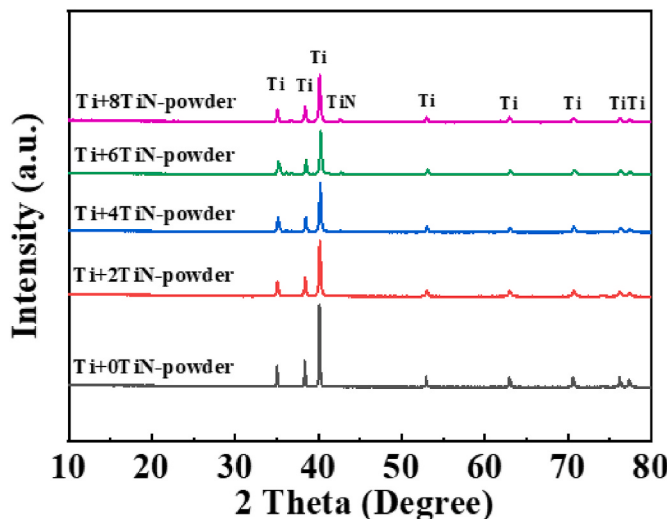


Fig. 3. The XRD patterns of the mixed Ti and TiN powders.

**Table 1**  
N, O, H, C contents of the sintered samples with different addition of TiN.

Material	N		O		H		C	
	(wt %)	(at %)						
Ti + 0TiN	0.04	0.13	0.33	0.97	0.021	0.98	0.016	0.06
Ti + 2TiN	0.63	3.06	0.37	1.05	0.068	3.06	0.015	0.06
Ti + 4TiN	1.28	4.00	0.36	0.98	0.12	5.21	0.016	0.06
Ti + 6TiN	1.84	5.67	0.41	1.11	0.12	5.14	0.016	0.06
Ti + 8TiN	2.66	8.41	0.35	0.97	0.019	0.84	0.018	0.07

regions indicate the indices of the (0001), (01 1(-) 0), and (1(-) 21(-) 0) crystal planes, respectively. With increasing solute concentration of the N atoms, the crystal orientations of all five samples were distributed uniformly, and no basal textures or twin structures were found. Fig. 6 shows the average grain sizes calculated using EBSD. This illustrates that the crystal orientation had a minimal effect on the mechanical strength of the sintered samples. The grain sizes of all five sintered samples decreased from 14.6  $\mu\text{m}$  to 6.0  $\mu\text{m}$ , which suggests that the addition of

TiN refines the grain size. However, the changes in the grain sizes were minor, and the contributions of fine-grain strengthening to the overall strength were slight according to the Hall-Petch equation. The strengthening mechanisms of the Ti–N alloy are discussed hereinafter.

Fig. 7(a) illustrates the strain–stress curves for each sintered sample. The physical and mechanical properties, including the density, yield strength ( $\sigma_y$ ), elongation ( $\epsilon$ ), and Young's modulus ( $E$ ), are listed in Table 2. The density of all the sintered samples was approximately 4.51 g/cm<sup>3</sup>, which is the same as that of CP-Ti, which demonstrates that after processing by this method, the sintered samples were generally compact without hot extrusion. The Young's moduli were 118, 122, 131, 132, and 135 GPa for Ti + 2TiN, Ti + 4TiN, Ti + 6TiN, and Ti + 8TiN, respectively, following an increasing trend with increasing N content, as expected. This result is consistent with a prior report that interstitial  $\alpha$ -stabilizing solutes tended to increase the Young's modulus [25,37]. In addition, both the yield strength and ultimate compressive strength increased dramatically and linearly with increasing nitrogen concentration. The Ti + 0TiN specimen did not fracture in the compressive test, owing to its excellent plasticity. As shown in Fig. 7(a), the compressive yield strength reached 596 MPa, and the sample did not fracture when the compressive strain exceeded 40%. The compressive yield strength and elongation were 933 MPa and 29.59% for Ti + 2TiN, 1187 MPa and 14.08% for Ti + 4TiN, 1498 MPa and 7.91% for Ti + 6TiN, and 2012 MPa and 1.35% for Ti + 8TiN. Moreover, for the Ti + 2TiN sample with the lowest addition of TiN and a N content of 0.63 wt%, the compressive yield strength exceeded most of the commercial titanium alloys [38–45], with an elongation of almost 30%. With increasing TiN content, the compressive yield strength of the Ti–N alloys increased significantly, and surpassed other commercial titanium alloys.

The fracture surfaces of the specimens were observed by SEM. Fig. 8 displays the fracture surface morphology of all sintered samples, along with their respective high-magnification images. Cleavages and dimples were observed in all the investigated alloys except for Ti + 0TiN, because the alloys did not fracture. The dimples are highlighted in the figure, where the density of the dimples decreased with an increase in the N content. A higher magnification image of the dimples in each sample is also shown on the corner of each image.

## 4. Discussion

### 4.1. Location of the N atoms

To determine the location of the N atoms in Ti, the XRD data presented in Fig. 4 were analyzed. The shift of the (0002)  $\alpha$ -Ti peak to a lower diffraction angle with increasing N content revealed that the

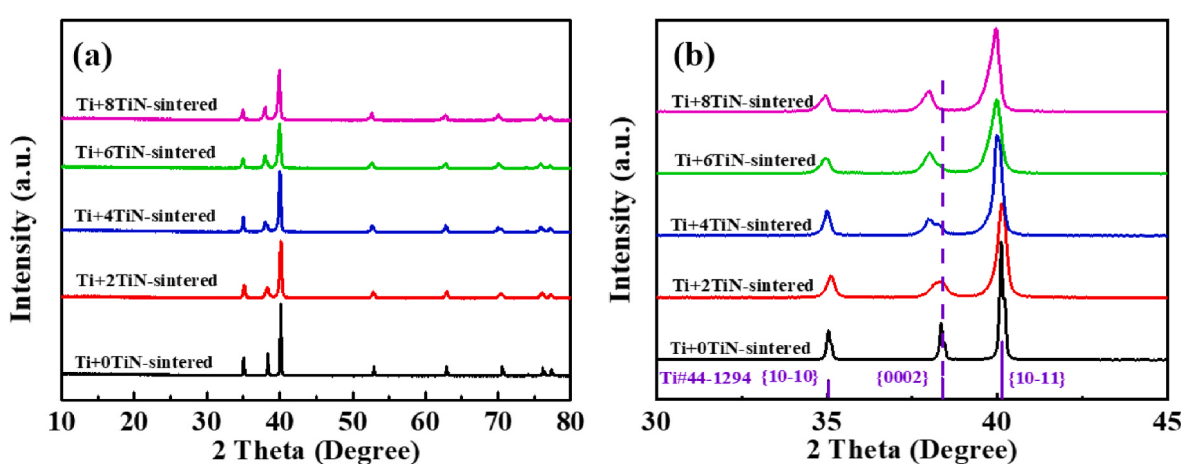
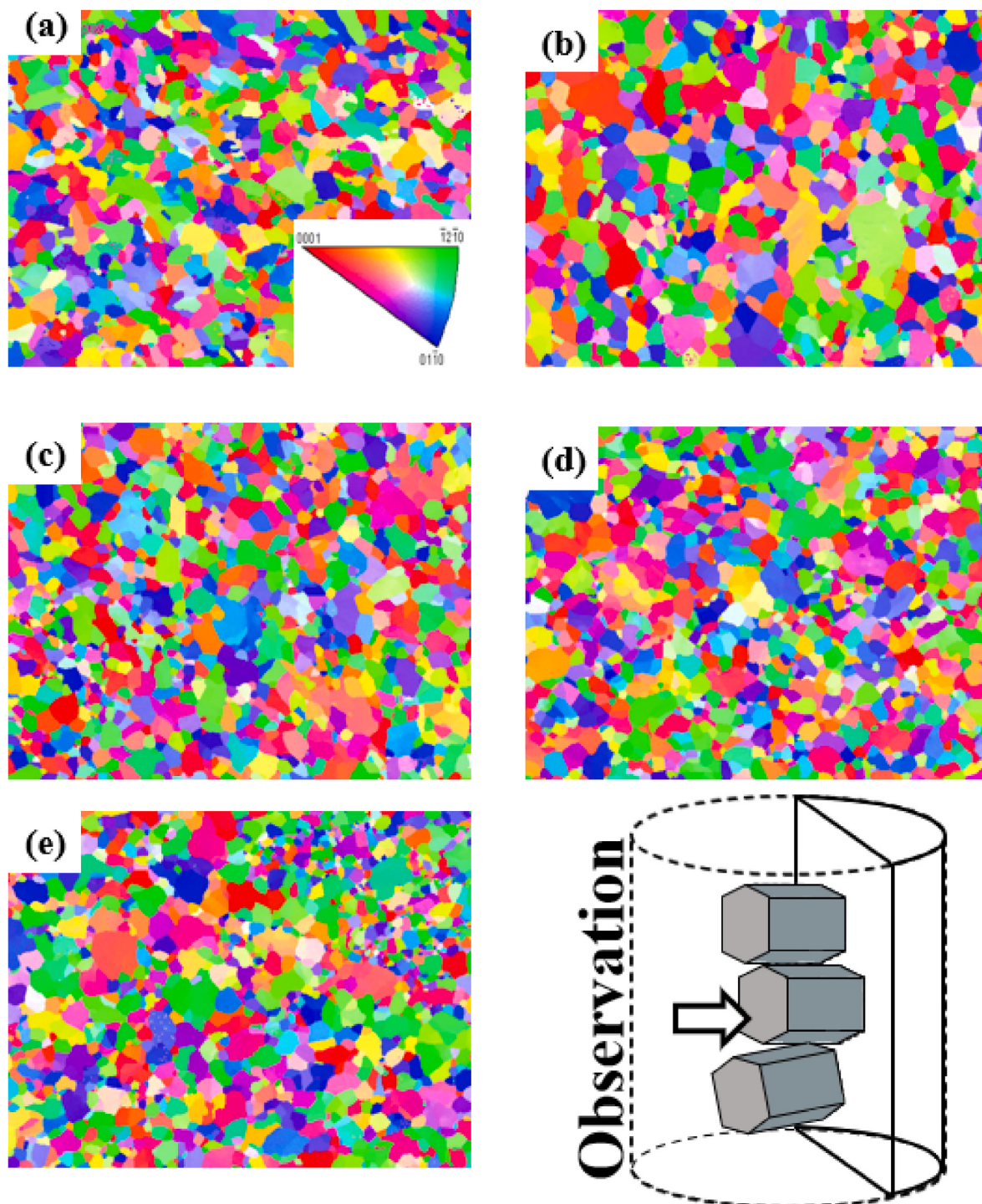


Fig. 4. XRD patterns of the sintered samples with different addition of the TiN (a) XRD patterns with a two-theta angle range from 10° to 80°, (b) local XRD patterns with a two-theta angle range from 30° to 45° that demonstrates the peak shift to the lower angle.



**Fig. 5.** IPF maps of (a) Ti + 0TiN, (b) Ti + 2TiN, (c) Ti + 4TiN, (d) Ti + 6TiN, (e) Ti + 8TiN.

dissolved N atoms led to lattice expansion along the c-axis. The (10 1 $\bar{1}$ )  $\alpha$ -Ti peak did not shift, which means that the dissolved N atoms do not distort the a-axis. The lattice parameters along the a- and c-axes were calculated using Bragg's law [31], as shown in Fig. 9(a). The lattice parameters along the a- and c-axes for pure titanium were 2.953 Å and 4.688 Å, respectively. With increasing addition of TiN, the lattice spacing along the c-axis increased significantly from 4.688 Å to 4.710 Å, while the lattice spacing along the a-axis increased slightly from 2.953 Å to 2.957 Å. The c/a ratio also increased from 1.588 to 1.592. The N atoms dissolved in the  $\alpha$ -Ti matrix at the octahedral interstice via SPS are schematically represented in Fig. 9(b). The XRD data are also consistent

with the first principles prediction that interstitial diffusion of N in  $\alpha$ -Ti at the octahedral interstice is the most stable, where this arrangement has the lowest interstitial energy [46].

#### 4.2. Analysis of fracture modes

The fracture surfaces of the specimens were studied to analyze the deformation behavior and failure mechanism (Fig. 8). For HCP-structured metals, the principal slip plane is strongly correlated with the c/a ratio [47]. When the c/a ratio was larger than 1.61, basal plane slipping occurred in the long HCP structure; otherwise, prismatic plane

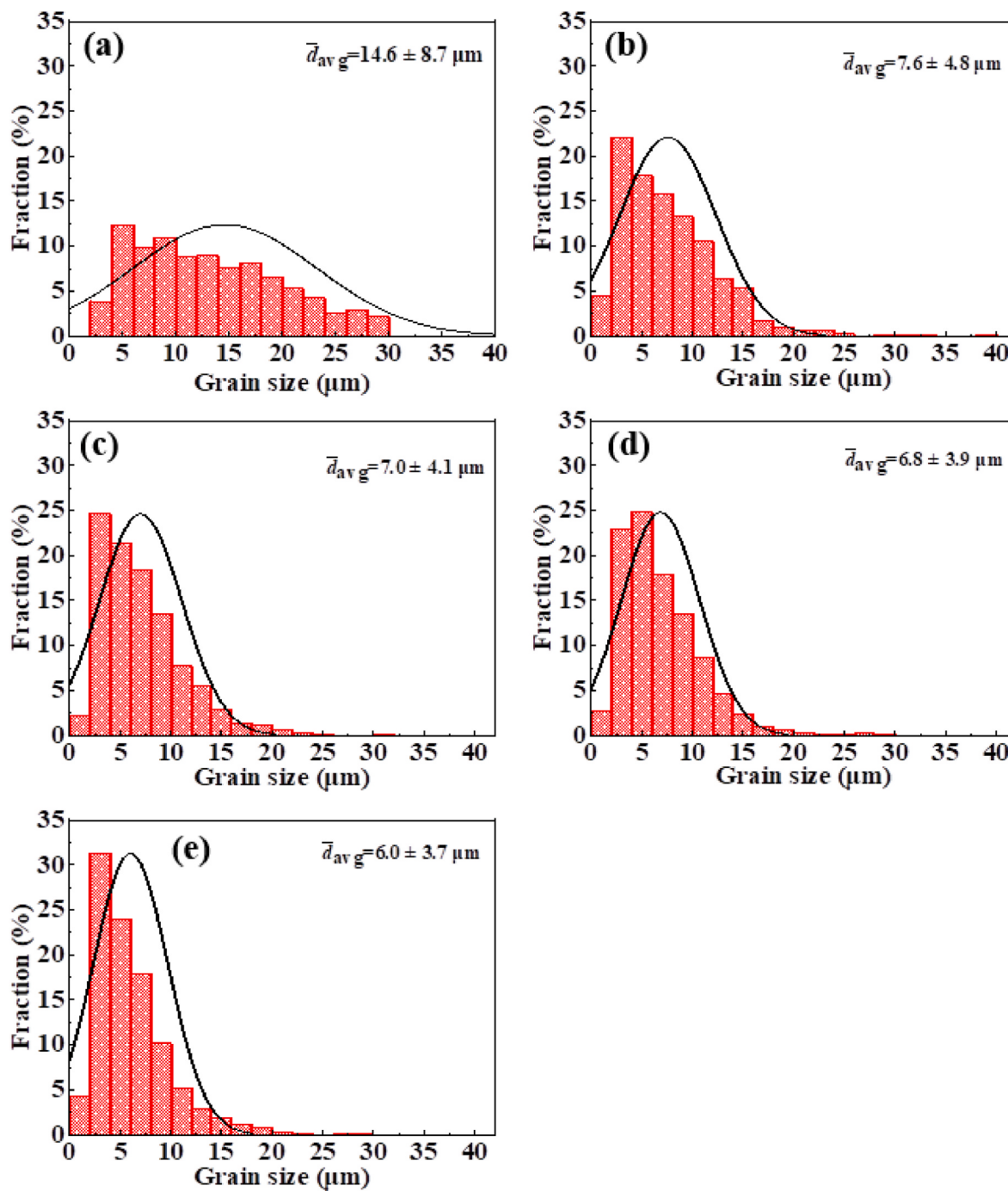


Fig. 6. Grain size distributions calculated from the EBSD data of (a) Ti + 0TiN, (b) Ti + 2TiN, (c) Ti + 4TiN, (d) Ti + 6TiN, (e) Ti + 8TiN.

slipping was dominant in the short HCP structure. The c/a ratio of the sintered samples increased slightly with increasing concentration of the dissolved atoms. The c/a ratio was approximately 1.59, indicating that the principal slip plane was the prismatic plane, which is in agreement with the fact that the most easily activated slip system for  $\alpha$ -Ti is prismatic slip [48]. When the compressive direction was perpendicular to the glide plane, cleavage fracture occurred.

On the other hand, dimple fracture, which competes with cleavage fracture, also occurred in all four samples [49]. In general, dimpled features are caused by plastic instability [50]. Therefore, the morphology of the dimpled features represents the level of plastic deformation. When the amount of N atoms reached 2.66 wt%, dimple features were observed, indicating that the Ti-N alloys maintained

ductility when the yield strength reached 2000 MPa. In addition, with increasing dissolution of the N atoms, the density of the dimple features decreased, leading to reduced plasticity [51]. This result is in close agreement with the stress-strain curves.

#### 4.3. Quantitative analysis of strengthening mechanisms

In this study, the primary strengthening mechanism discussed and analyzed is solution hardening by N atoms dissolved in the  $\alpha$ -Ti matrix. The N atoms, as the interstitial atoms, were located in the octahedral interstices [52]. These N atoms played the role of an obstacle, which had a pinning control on the movement of dislocations [53,54]. Furthermore, under applied stress, the dislocations require more energy by

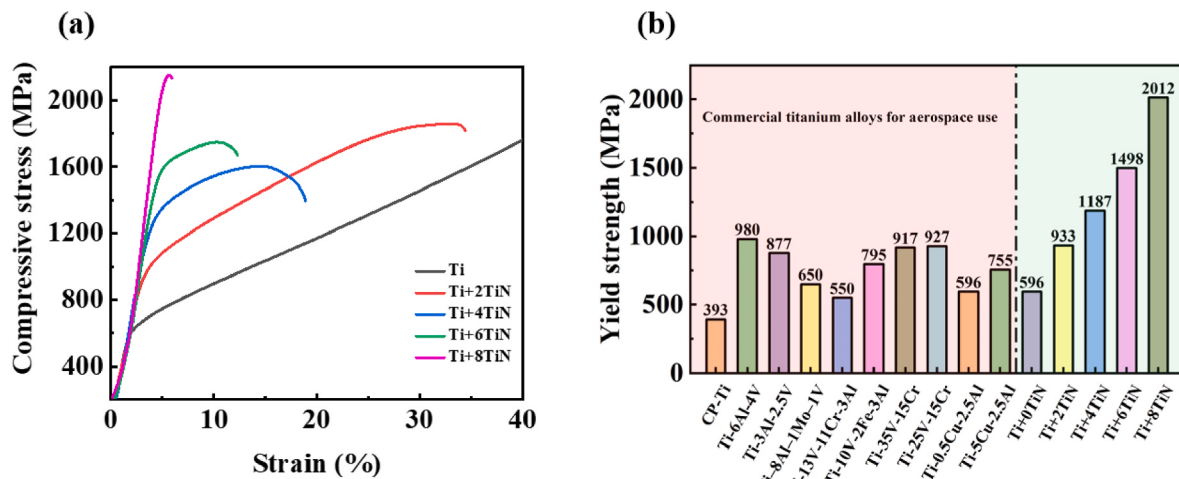


Fig. 7. Mechanical behavior (a) Compressive stress-strain curves, (b) Compressive yield strength of commercial titanium alloys and our samples.

**Table 2**  
Physical and mechanical properties of these Ti–N alloys.

Material	Density (g/cm <sup>3</sup> )	$\sigma_y$ (MPa)	$\epsilon$ (%)	E (GPa)
Ti + 0TiN	4.51	596	–	118
Ti + 2TiN	4.51	933	29.59	122
Ti + 4TiN	4.51	1187	14.08	131
Ti + 6TiN	4.51	1498	7.91	132
Ti + 8TiN	4.51	2012	1.35	135

applying anisotropic strain to overcome the lattice distortion caused by the N atoms [55]. In addition to the N solid solution strengthening effect, other strengthening mechanisms are operative in metals. Microstructural and atomic-scale influences were considered to analyze the mechanical improvements caused by other factors.

To study the influence of the microstructure on the strength of the alloy, the grain sizes of the sintered Ti–N alloys were analyzed. Generally, metals with a finer grain microstructure have greater strength [56]. However, when the grain size is small, the relationship between the grain size and yield strength is defined by the Hall-Petch equation as follows [57,58]:

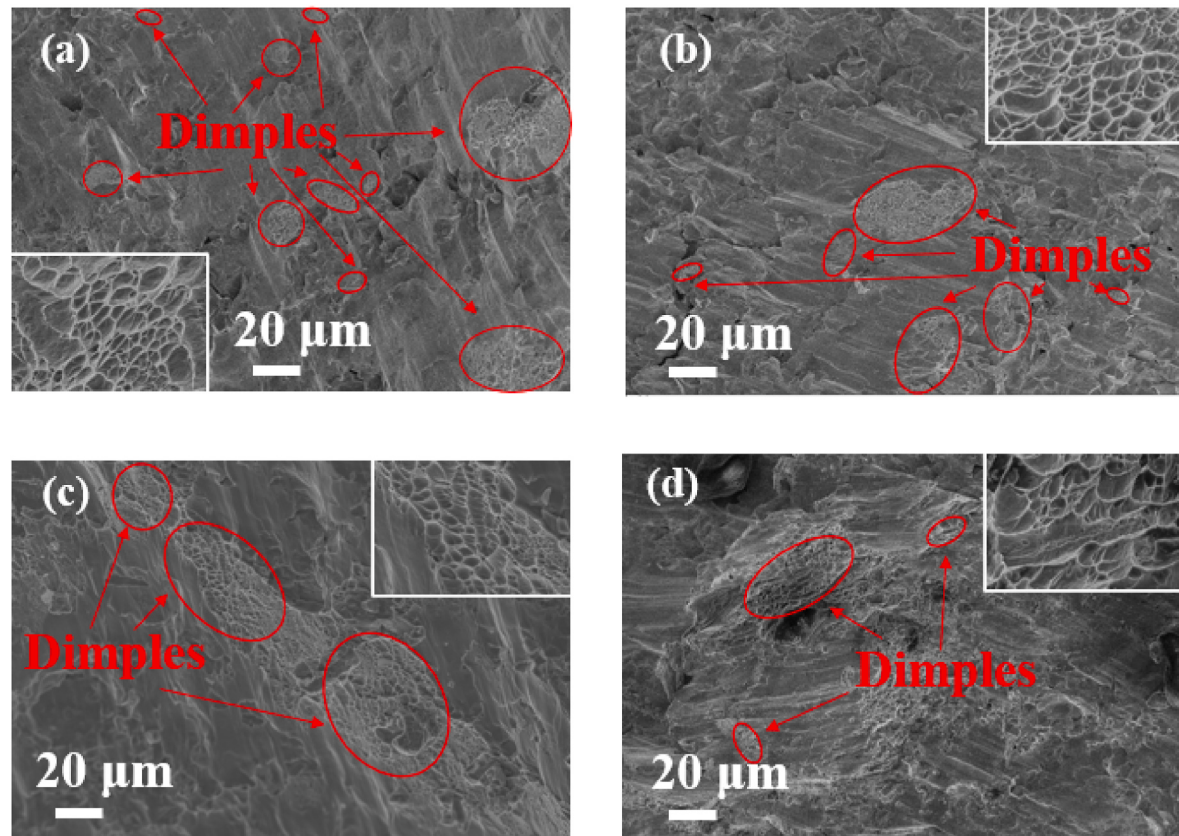
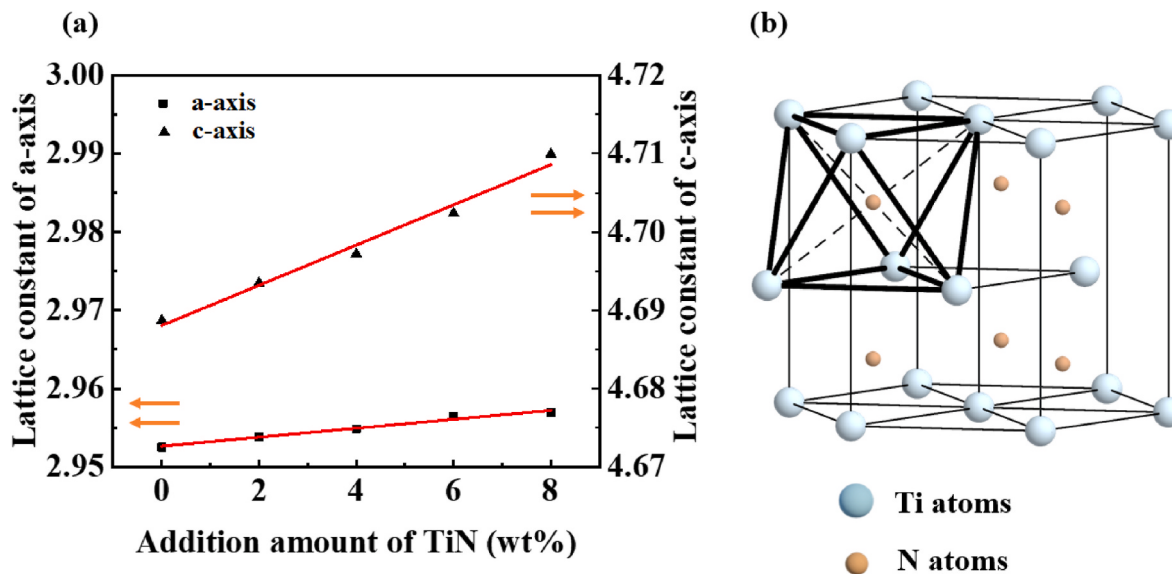


Fig. 8. SEM images of the fractured surfaces after compression test of (a) Ti + 2TiN, (b) Ti + 4TiN, (c) Ti + 6TiN, (d) Ti + 8TiN.



**Fig. 9.** (a) The lattice parameters of the a-axis and c-axis of the Ti–N alloys calculated from the XRD peak shifts, (b) the schematic diagram of the Ti–N alloys.

$$\sigma_{ys(HP)} = \sigma_0 + kd^{-0.5}$$

where  $\sigma_0$  is a material constant for the starting stress for dislocation movement,  $k$  is the Hall-Petch coefficient, and  $d$  is the mean grain size of the Ti–N alloys. Because the  $\sigma_0$  values of the Ti–N alloys were the same as those of pure Ti, the increase in the compressive strength due to the grain refinement effect could be estimated as follows:

$$\Delta\sigma_{ys(HP)} = k(d_0^{-0.5} - d^{-0.5})$$

where  $d_0$  is the mean grain size of pure Ti. The grain size was determined by EBSD as mentioned before, where  $k$  is 18.6 MPa/mm<sup>-0.5</sup>, according to previous work [59].

On the atomic scale, the dissolved atoms, including the interstitial or substitutional atoms, significantly affect the yield strength of the alloy. Therefore, the increase in the yield strength caused by the interaction between dislocations and solute atoms is positively correlated with the content of solute atoms. In general, a typical model for solid solute strengthening is the Labusch model [60]:

$$\Delta\sigma_{ys(SS)} = \frac{\tau}{S_F} = \frac{c^{2/3}}{S_F} \left( \frac{F_m^4 w}{4Gb^9} \right)^{1/3}$$

where  $c$  is the atomic ratio of the interstitial atoms,  $S_F$  is the Schmid factor measured by EBSD analysis of each sintered sample,  $F_m$  is the maximum interaction force,  $w$  is the width of the edge dislocation,  $G$  is the shear modulus, and  $b$  is the Burgers vector. As indicated by analyzing the content of several elements, O atoms are also major solute atoms, in addition to the N atoms. These elements were quantitatively analyzed to study the contributions of O atoms to the yield strength ( $\Delta\sigma_{ys(O-SS)}$ ).  $S_F$  can be calculated from the EBSD data. However, the  $F_m$  value is difficult to determine because of the anisotropic strain and stress applied by the solid solute atoms. Several studies have assumed the  $F_m$  and  $(F_m^4 w / 4Gb^9)^{1/3}$  value of Ti–O to be  $6.22 \times 10^{-10}$  N and  $4.17 \times 10^{-3}$  [61], which will be used in this study. For the  $(F_m^4 w / 4Gb^9)^{1/3}$  value of Ti–N, the slope of the linear relationship between the yield increment by the N atoms and  $(c^{2/3} / S_F)$  is shown in Table 3.

The results show that the increase in the grain refinement strengthening was slight (approximately 30 MPa), whereas the strengthening effect caused by the solute N atoms was significant. To some extent, the solute O atoms also affect the yield strength, but the content of O in all the sintered samples was the same, which results in the same

contribution by the O atoms. Consequently, the N atoms introduced by the TiN powder remarkably increased the yield strength of the Ti–N alloy.

## 5. Conclusions

Ultra-high-strength Ti alloys with high N solute atom contents were successfully fabricated via the PM process. The microstructure, compressive performance, and deformation behavior of the Ti alloys were studied. The conclusions are as follows:

- (1) No noticeable chemical reactions occurred during the ball-milling process used to mix the pure Ti and TiN powders. TiN decomposed completely and the N atoms dissolved in the octahedral interstice of the sintered Ti–N alloys after ball-milling and SPS.
- (2) The yield strength of the Ti–N alloys increased with increasing N content, reaching 2012 MPa when the N content was 2.66 wt%. Analysis of the fracture features indicated synergism between microporous polymeric and cleavage fractures, where cleavage fracture became dominant as the N content increased.
- (3) According to quantitative analysis, the main strengthening mechanisms of the sintered Ti–N alloys were solution strengthening by the N and O atoms and fine-grain strengthening.

## CRediT authorship contribution statement

Jiayin Chen: Did the experiment, Analyzed the data and wrote the

**Table 3**

Grain size, Schmid factor, yield strength, and the increment from grain refinement and solute atoms.

Material	Ti + 0TiN	Ti + 2TiN	Ti + 4TiN	Ti + 6TiN	Ti + 8TiN
Grain size (μm)	12.6	7.6	7.0	6.8	6.0
$\Delta\sigma_{ys(HP)}$	–	14.7	16.8	17.5	20.4
Schmid factor	0.389	0.389	0.389	0.390	0.381
$\Delta\sigma_{ys(N-SS)}$	–	322.4	530.4	856.0	1387.4
$\Delta\sigma_{ys(O-SS)}$	–	25.8	2.6	42.8	9.0
Theoretical increment	–	959	1146	1512	2013
Yield strength (MPa)	596	933	1187	1498	2012

paper. **Zeyun Cai:** Responsible for the alloy preparation and analyzed the data. **Tao Xiang:** Responsible for the alloy preparation and analyzed the data. **Peng Du:** Responsible for the alloy preparation and analyzed the data. **Guoqiang Xie:** Conceived the idea, Designed the experiment and wrote the paper. All the authors discussed the result, revised the paper, and approved the final version.

## Declaration of competing interest

The authors declare that they have no known competing financial interests or personal relationships that could have appeared to influence the work reported in this paper.

## Acknowledgements

The work was financially supported by Guangdong Basic and Applied Basic Research Foundation (No. 2021A1515012626), the National Natural Science Foundation of China (No. 51871077), the Shenzhen Knowledge Innovation Plan-Fundamental Research (Discipline Distribution) (No. JCYJ20180507184623297), the Development and Reform Commission of Shenzhen Municipality-Shenzhen R&D Center for AI-based Hydrogen Hydrolysis Materials (No. ZX20190229), the Startup Foundation from Shenzhen and Startup Foundation from Harbin Institute of Technology (Shenzhen).

## References

- [1] X.Y. Liu, P.K. Chu, C.X. Ding, Surface modification of titanium, titanium alloys, and related materials for biomedical applications, *Mater. Sci. Eng., A* 47 (2004) 49–121, <https://doi.org/10.1016/j.msea.2004.11.001>.
- [2] M. Geetha, A.K. Singh, R. Asokamani, A.K. Gogia, Ti based biomaterials, the ultimate choice for orthopaedic implants - a review, *Prog. Mater. Sci.* 54 (2009) 397–425, <https://doi.org/10.1016/j.pmatsci.2008.06.004>.
- [3] D. Banerjee, J.C. Williams, Perspectives on titanium science and technology, *Acta Mater.* 61 (2013) 844–879, <https://doi.org/10.1016/j.actamat.2012.10.043>.
- [4] Y.L. Hao, S.J. Li, R. Yang, Biomedical titanium alloys and their additive manufacturing, *Rare Met.* 35 (2016) 661–671, <https://doi.org/10.1007/s12598-016-0793-5>.
- [5] X.S. Zhang, Y.J. Chen, J.L. Hu, Recent advances in the development of aerospace materials, *Prog. Aero. Sci.* 97 (2018) 22–34, <https://doi.org/10.1016/j.paerosci.2018.01.001>.
- [6] R.R. Boyer, Attributes, characteristics, and applications of titanium and its alloys, *JOM* 62 (2010) 21–24, <https://doi.org/10.1007/s11837-010-0071-1>.
- [7] M. Peters, J. Kumpfert, C.H. Ward, C. Leyens, Titanium alloys for aerospace applications, *Adv. Eng. Mater.* 5 (2003) 419–427, <https://doi.org/10.1002/adem.200310095>.
- [8] A.K. Singla, M. Banerjee, A. Sharma, J. Singh, A. Bansal, M.K. Gupta, N. Khanna, A. S. Shahi, D.K. Goyal, Selective laser melting of Ti6Al4V alloy: process parameters, defects and post-treatments, *J. Manuf. Process.* 64 (2021) 161–187, <https://doi.org/10.1016/j.jmapro.2021.01.009>.
- [9] L. Narayan, Aerospace materials market by type (aluminium alloys, steel alloys, titanium alloys, super alloys, and composite materials), aircraft type (commercial aircraft, business & general aviation, helicopters), and region - global forecast to 2022, accessed September 2021), <https://www.marketsandmarkets.com/Market-Reports/aerospace-materials-market-266342713.html>, 2017.
- [10] T. Zhu, J. Li, Ultra-strength materials, *Prog. Mater. Sci.* 55 (2010) 710–757, <https://doi.org/10.1016/j.pmatsci.2010.04.001>.
- [11] S. Suresh, J. Li, Materials science deformation of the ultra-strong, *Nature* 456 (2008) 716–717, <https://doi.org/10.1038/456716a>.
- [12] S.L. Semiatin, P.A. Kobrynn, E.D. Roush, D.U. Furrer, T.E. Howson, R.R. Boyer, D. J. Chellman, Plastic flow and microstructure evolution during thermomechanical processing of laser-deposited Ti-6Al-4V preforms, *Metall. Mater. Trans. A* 32 (2001) 1801–1811, <https://doi.org/10.1007/s11661-001-0156-0>.
- [13] Z.Z. Fang, J.D. Paramore, P. Sun, K.S.R. Chandran, Y. Zhang, Y. Xia, F. Cao, M. Koopman, M. Free, Powder metallurgy of titanium - past, present, and future, *Int. Mater. Rev.* 63 (2018) 407–459, <https://doi.org/10.1080/09506608.2017.1366003>.
- [14] M. Gepreel, M. Niinomi, Biocompatibility of Ti-alloys for long-term implantation, *J. Mech. Behav. Biomed. Mater.* 20 (2013) 407–415, <https://doi.org/10.1016/j.jmbbm.2012.11.014>.
- [15] P. Du, Z.W. Wu, K. Li, T. Xiang, G.Q. Xie, Porous Ti-based bulk metallic glass orthopedic biomaterial with high strength and low Young's modulus produced by one step SPS, *J. Mater. Res. Technol.* 13 (2021) 251–259, <https://doi.org/10.1016/j.jmrt.2021.04.084>.
- [16] G.Q. Xie, H. Kanetaka, H. Kato, F.X. Qin, W. Wang, Porous Ti-based bulk metallic glass with excellent mechanical properties and good biocompatibility, *Intermetallics* 105 (2019) 153–162, <https://doi.org/10.1016/j.intermet.2018.12.002>.
- [17] E.O. Ezugwu, Z.M. Wang, Titanium alloys and their machinability - a review, *J. Mater. Process. Technol.* 68 (1997) 262–274, [https://doi.org/10.1016/s0924-0136\(96\)00030-1](https://doi.org/10.1016/s0924-0136(96)00030-1).
- [18] J. Shen, B. Chen, J. Umeda, K. Kondoh, Advanced mechanical properties of a powder metallurgy Ti-Al-N alloy doped with ultrahigh nitrogen concentration, *JOM* 70 (2018) 626–631, <https://doi.org/10.1007/s11837-018-2780-9>.
- [19] L.S. Wei, H.Y. Kim, T. Koyano, S. Miyazaki, Effects of oxygen concentration and temperature on deformation behavior of Ti-Nb-Zr-Ta-O alloys, *Scripta Mater.* 123 (2016) 55–58, <https://doi.org/10.1016/j.scriptamat.2016.05.043>.
- [20] A. Issariyapat, P. Visuttipitkul, T.T. Song, A. Bahador, J. Umeda, M. Qian, K. Kondoh, Tensile properties improvement by homogenized nitrogen solid solution strengthening of commercially pure titanium through powder metallurgy process, *Mater. Char.* 170 (2020), 110700, <https://doi.org/10.1016/j.matchar.2020.110700>.
- [21] Z.F. Lei, X.J. Liu, Y. Wu, H. Wang, S.H. Jiang, S.D. Wang, X.D. Hui, Y.D. Wu, B. Gault, P. Kontis, D. Raabe, L. Gu, Q.H. Zhang, H.W. Chen, H.T. Wang, J.B. Liu, K. An, Q.S. Zeng, T.G. Nieh, Z.P. Lu, Enhanced strength and ductility in a high-entropy alloy via ordered oxygen complexes, *Nature* 563 (2018) 546–553, <https://doi.org/10.1038/s41586-018-0685-y>.
- [22] T. Ando, K. Nakashima, T. Tsuchiyama, S. Takaki, Microstructure and mechanical properties of a high nitrogen titanium alloy, *Mater. Sci. Eng., A* 486 (2008) 228–234, <https://doi.org/10.1016/j.msea.2007.08.074>.
- [23] W.H. Yin, F. Xu, O. Ertorer, Z. Pan, X.Y. Zhang, L.J. Kecske, E.J. Lavernia, Q. Wei, Mechanical behavior of microstructured engineered multi-length-scale titanium over a wide range of strain rates, *Acta Mater.* 61 (2013) 3781–3798, <https://doi.org/10.1016/j.actamat.2013.03.011>.
- [24] J. Shen, B. Chen, J. Umeda, K. Kondoh, Microstructure and mechanical properties of CP-Ti fabricated via powder metallurgy with non-uniformly dispersed impurity solutes, *Mater. Sci. Eng., A* 716 (2018) 1–10, <https://doi.org/10.1016/j.msea.2018.01.031>.
- [25] H. Conrad, Effect of interstitial solutes on the strength and ductility of titanium, *Prog. Mater. Sci.* 26 (1981) 123–404, [https://doi.org/10.1016/0079-6425\(81\)90001-3](https://doi.org/10.1016/0079-6425(81)90001-3).
- [26] Z.Y. Cai, J.Y. Chen, P. Du, T. Xiang, J. Chen, G.Q. Xie, Mechanical behavior and microstructure control of the low-cost titanium-oxygen alloy prepared by ball milling and spark plasma sintering, *J. Alloys Compd.* 887 (2021), 161349, <https://doi.org/10.1016/j.jallcom.2021.161349>.
- [27] X. Wang, J. Li, F. Cazes, A. Hocini, G. Dirras, Numerical modeling on strengthening mechanisms of the harmonic structured design on CP-Ti and Ti-6Al-4V, *Int. J. Plast.* 133 (2020), 102793, <https://doi.org/10.1016/j.ijplas.2020.102793>.
- [28] T. Mimoto, J. Umeda, K. Kondoh, Titanium powders via gas-solid direct reaction process and mechanical properties of their extruded materials, *Mater. Trans.* 56 (2015) 1153–1158, <https://doi.org/10.2320/matertrans.L-M2015816>.
- [29] Z.A. Munir, 1000 at 1000: the effect of electric field and pressure on the synthesis and consolidation of materials: a review of the spark plasma sintering method, *J. Mater. Sci.* 55 (2020) 15365–15366, <https://doi.org/10.1007/s10853-020-05040-4>.
- [30] G.Q. Xie, D.V. Louguine-Luzgin, L. Song, H. Kimura, A. Inoue, Dual phase metallic glassy composites with large-size and ultra-high strength fabricated by spark plasma sintering, *Intermetallics* 17 (2009) 512–516, <https://doi.org/10.1016/j.intermet.2009.01.003>.
- [31] A.A. Bunaciu, E.G. Udristioiu, H.Y. Aboul-Enein, X-ray diffraction: instrumentation and applications, *Crit. Rev. Anal. Chem.* 45 (2015) 289–299, <https://doi.org/10.1080/10408347.2014.949616>.
- [32] A. Issariyapat, P. Visuttipitkul, T.T. Song, J. Umeda, M. Qian, K. Kondoh, Strength-ductility improvement of extruded Ti-(N) materials using pure Ti powder with high nitrogen solution, *Mater. Sci. Eng., A* 779 (2020), 139136, <https://doi.org/10.1016/j.msea.2020.139136>.
- [33] M. Omori, Sintering, consolidation, reaction and crystal growth by the spark plasma system (SPS), *Mater. Sci. Eng., A* 287 (2000) 183–188, [https://doi.org/10.1016/s0921-5093\(00\)00773-5](https://doi.org/10.1016/s0921-5093(00)00773-5).
- [34] A.M. Roy, Multiphase phase-field approach for solid-solid phase transformations via propagating interfacial phase in HMX, *J. Appl. Phys.* 129 (2021), 025103, <https://doi.org/10.1063/5.0025867>.
- [35] A.M. Roy, Energetics and kinematics of undercooled nonequilibrium interfacial molten layer in cyclotetramethylene-tetrannitrilic crystal, *Physica B (Amsterdam, Neth.)* 615 (2021), 412986, <https://doi.org/10.1016/j.physb.2021.412986>.
- [36] N.R. McDonald, G.R. Wallwork, The reaction of nitrogen with titanium between 800 and 1200°C, *Oxid. Metals* 2 (1970) 263–283, <https://doi.org/10.1007/BF00614621>.
- [37] Z. Trojanova, P.A. Maksimiyuk, P. Lukac, Temperature-dependence of Young's modulus of alpha-titanium polycrystals, *Phys. Status Solidi A* 143 (1994) K75–K77, <https://doi.org/10.1002/pssa.2211430238>.
- [38] Y. Alshammari, F. Yang, L. Bolzoni, Fabrication and characterisation of low-cost powder metallurgy Ti-xCu-2.5Al alloys produced for biomedical applications, *J. Mech. Behav. Biomed. Mater.* 126 (2022), 105022, <https://doi.org/10.1016/j.jmbbm.2021.105022>.
- [39] Y.Q. Zhao, H.L. Qu, M.M. Wang, H. Wu, K.Y. Zhu, Thermal stability and creep behavior of Ti-V-Cr burn-resistant alloys, *J. Alloys Compd.* 407 (2006) 118–124, <https://doi.org/10.1016/j.jallcom.2005.06.014>.
- [40] L. Qi, X. Qiao, L. Huang, X. Huan, X. Zhao, Effect of structural stability on the stress induced martensitic transformation in Ti-10V-2Fe-3Al alloy, *Mater. Sci. Eng., A* 756 (2019) 381–388, <https://doi.org/10.1016/j.msea.2019.04.058>.
- [41] M. Jia, B. Gabbitas, Rapid synthesis of a near-beta titanium alloy by blended elemental powder metallurgy (BEPM) with induction sintering, *Mater. Trans. A* 46A (2015) 4716–4729, <https://doi.org/10.1007/s11661-015-3048-4>.

- [42] I.G. Dastidar, V. Khademi, T.R. Bieler, A.L. Pilchak, M.A. Crimp, C.J. Boehlert, The tensile and tensile-creep deformation behavior of Ti-8Al-1Mo-1V(wt%), Mater. Sci. Eng., A 636 (2015) 289–300, <https://doi.org/10.1016/j.msea.2015.03.059>.
- [43] M. Miller, T. Chavez, M. Dearborn, E. Tong, E. Devore, R. Marloth, Y.-J. Li, L. Zeng, B. Ramsey, H. Mulazimoglu, J. Guerra, J. Foyos, N. Ula, H. Garmestani, O.S. Es-Said, Effect of heat treatments on the mechanical properties of Ti-3Al-2.5V alloy, J. Mater. Eng. Perform. 24 (2015) 3277–3290, <https://doi.org/10.1007/s11665-015-1628-5>.
- [44] P. Wang, L. Wu, Y. Feng, J. Bai, B. Zhang, J. Song, S. Guan, Microstructure and mechanical properties of a newly developed low Young's modulus Ti-15Zr-5Cr-2Al biomedical alloy, Mater. Sci. Eng., C 72 (2017) 536–542, <https://doi.org/10.1016/j.msec.2016.11.101>.
- [45] Y. Hao, J. Liu, J. Li, S. Li, Q. Zou, X. Chen, Rapid preparation of TiC reinforced Ti6Al4V based composites by carburizing method through spark plasma sintering technique, Mater. Des. 65 (2015) 94–97, <https://doi.org/10.1016/j.matdes.2014.09.008>.
- [46] L. Scotti, A. Mottura, Interstitial diffusion of O, N, and C in alpha-Ti from first-principles: analytical model and kinetic Monte Carlo simulations, J. Chem. Phys. 144 (2016), 084701, <https://doi.org/10.1063/1.4942030>.
- [47] I.P. Jones, W.B. Hutchinson, Stress-state dependence of slip in titanium-6Al-4V and other HCP metals, Acta Metall. 29 (1981) 951–968, [https://doi.org/10.1016/0001-6160\(81\)90049-3](https://doi.org/10.1016/0001-6160(81)90049-3).
- [48] L. Wang, Z. Zheng, H. Phukan, P. Kenesei, J.S. Park, J. Lind, R.M. Suter, T.R. Bieler, Direct measurement of critical resolved shear stress of prismatic and basal slip in polycrystalline Ti using high energy X-ray diffraction microscopy, Acta Mater. 132 (2017) 598–610, <https://doi.org/10.1016/j.actamat.2017.05.015>.
- [49] M.C. Brandes, M. Baughman, M.J. Mills, J.C. Williams, The effect of oxygen and stress state on the yield behavior of commercially pure titanium, Mater. Sci. Eng., A 551 (2012) 13–18, <https://doi.org/10.1016/j.msea.2012.04.058>.
- [50] L. Chang, C.Y. Zhou, X.H. He, The effects of prestrain and subsequent annealing on tensile properties of CP-Ti, Metals 7 (2017) 99, <https://doi.org/10.3390/met7030099>.
- [51] W.W. Gerberich, K. Jatavallabhula, Quantitative fractography and dislocation interpretations of the cyclic cleavage crack-growth process, Acta Metall. 31 (1983) 241–255, [https://doi.org/10.1016/0001-6160\(83\)90101-3](https://doi.org/10.1016/0001-6160(83)90101-3).
- [52] Y. Du, B. Zhang, C. You, W. Zhang, Y. Li, Y. Zhang, Strengthening and toughening mechanisms of titanium-nitrogen alloy with a laminated structure fabricated by spark plasma sintering, Mater. Sci. Eng., A 769 (2020), 138492, <https://doi.org/10.1016/j.msea.2019.138492>.
- [53] A.H. Cottrell, S.C. Hunter, F.R.N. Nabarro, Electrical interaction of a dislocation and a solute atom, Philos. Mag. A 44 (1953) 1064–1067, <https://doi.org/10.1080/14786441008520364>.
- [54] R.L. Fleischer, Substitutional solution hardening, Acta Metall. 11 (1963) 203–209, [https://doi.org/10.1016/0001-6160\(63\)90213-x](https://doi.org/10.1016/0001-6160(63)90213-x).
- [55] W.L. Finlay, J.A. Snyder, Effects of three interstitial solutes (nitrogen, oxygen, and carbon) on the mechanical properties of high-purity, alpha titanium, JOM 188 (1950) 277–286, <https://doi.org/10.1007/BF03399001>.
- [56] P. Luo, D.T. McDonald, W. Xu, S. Palanisamy, M.S. Dargusch, K. Xia, A modified Hall-Petch relationship in ultrafine-grained titanium recycled from chips by equal channel angular pressing, Scripta Mater. 66 (2012) 785–788, <https://doi.org/10.1016/j.scriptamat.2012.02.008>.
- [57] E.O. Hall, The deformation and ageing of mild steel: III, Proc. Phys. Soc. London, Sect. B 64 (1951) 747–753, <https://doi.org/10.1088/0370-1301/64/9/303>.
- [58] Y. Estrin, A. Vinogradov, Extreme grain refinement by severe plastic deformation: a wealth of challenging science, Acta Mater. 61 (2013) 782–817, <https://doi.org/10.1016/j.actamat.2012.10.038>.
- [59] K. Yuki, T. Yoshiteru, M. Kazuyoshi, K. Kazuhiro, M. Yoshiyuki, Effect of forging ratio and grain size on tensile and fatigue strength of pure titanium forgings, J. Soc. Mater. Sci., Jpn. 54 (2005) 66–72, <https://doi.org/10.2472/jSMS.54.66>.
- [60] R. Labusch, A statistical theory of solid solution hardening, Phys. Status Solidi A 41 (1970) 659–669, <https://doi.org/10.1002/pssa.19700410221>.
- [61] S. Kariya, M. Fukuo, J. Umeda, K. Kondoh, Quantitative analysis on light elements solution strengthening in pure titanium sintered materials by Labusch model using experimental data, Mater. Trans. 60 (2019) 263–268, <https://doi.org/10.2320/matertrans.Y-M2018849>.